Radar remote sensing retrieval of vertical profile of rainfall kinetic energy in the UK

Jingxuan Zhu, Qiang Dai, Yuanyuan Xiao, Jun Zhang, Lu Zhuo, and Dawei Han

***Abstract*—As rainfall undergoes a series of complex microphysical processes in the atmosphere, studying its vertical profiles is crucial for understanding the mechanisms of rainfall evolution. While previous research has focused on vertical profiles of rainfall intensity and drop size distribution (DSD) parameters, there remains a gap in the study of rainfall energy. This study uses the Dual-frequency Precipitation Radar (DPR) in Global Precipitation Measurement (GPM) to analyze the vertical profile characteristics of rainfall energy (KE_t) for the first time. Using DPR data collected from 2015 to 2022 across the UK, rainfall energy calculations reveal a strong correlation (over 0.99) between the rainfall energy of adjacent 125 m height bins, with stratiform rain showing higher correlation than convective rain. Specifically, below 1500 m, the correlation coefficient for KE_t in stratiform rain is 0.9973, while for convective rain it is 0.9957, showing higher KE_t variability in convective rain. The study also introduces the change ratio (R) to characterize the degree of change from the lower to upper height bins, finding that rainfall energy variability has a larger standard deviation compared to DSD parameters, with standard deviations for R mean values of KE_t reaching up to 28.37% for convective rain and 12.08% for stratiform rain within 1500 m. Additionally, the profiles of rainfall energy exhibit significant seasonal variations, with these variations increasing with height. KE_t is consistently highest in summer and lowest in winter at all same altitudes. This study enhances the understanding of the vertical pattern of rainfall evolution, contributes to providing more accurate surface rainfall energy estimates, analyzing influencing factors and the uncertainty of vertical rainfall variability.**

***Index Terms*—radar; remote sensing; DPR; vertical profile; rainfall energy**

I. INTRODUCTION

RAINFALL plays a crucial role in geography and environmental studies. It serves as a vital water supply, impacting ecosystems, agriculture, and human settlements [1], [2], [3], [4], [5]. Accurate estimation of rainfall patterns is essential for hydrometeorological studies [6], [7], enhancing our understanding of natural processes.

Apparent vertical precipitation structures exist in the atmosphere and are attributed to a series of microphysical processes (e.g., evaporation, drift, fragmentation and merging) carried out by raindrops [8], [9]. Therefore, the investigation of vertical precipitation profiles can facilitate a more comprehensive understanding of precipitation formation and evolution [10]. Additionally, this approach can provide more accurate surface precipitation information, particularly when remote sensing techniques are utilized [11]. The evolution of the microphysical processes of raindrops in the atmosphere has been investigated in the previous studies with techniques such as dense network of disdrometers, numerical weather prediction models and remote sensing [10], [12], [13], [14], [15].

However, rainfall energy, as one of the important characterizations of rainfall microphysics, is often neglected in current vertical profile studies. Rainfall energy refers to the kinetic energy that is converted from gravitational potential energy when raindrops land on the ground [16], [17]. It has a striking effect on soil aggregates and is a key driver of soil erosion [18], [19]. Rainfall energy is calculated by the drop size distribution (DSD) of raindrops and has a more complex vertical profile than rainfall intensity. In reality, the variation of the vertical profile of rainfall makes its characterization on the surface of different heights different. For example, the characteristics of raindrops at the top, the waist, and the bottom of the same mountain are different [10], [20]. Consequently, the accurate observation of the vertical profile of rainfall energy is necessary to revel the rainfall energy evolution pattern and the three-dimensional influencing elements, such as wind and pressure.

The current accurate rainfall energy measurements are mainly based on site disdrometer and weather radar. The disdrometer is the most accurate rainfall energy measurement instrument at present. This instrument analyzes signal changes from an impact or laser sensor to determine the size and velocity of raindrops within a given sampling range [17], [21]. Ground-based dual-polarization radar, on the other hand, is a means of acquiring rainfall energy at large scales. It realizes spatial and temporal retrieval of regional rainfall microphysical characteristics through information on the echo differences of distinct signals [16], [22], [23], [24].

Nevertheless, both disdrometer and ground-based weather radar have practical limitations in observing over widely

This work was supported by the National Natural Science Foundation of China under Grant 42371409 and 42201020. *(Corresponding author: Qiang Dai.)*

Jingxuan Zhu, Qiang Dai, Yuanyuan Xiao and Jun Zhang are with the Key Laboratory of Virtual Geographic Environment, Ministry of Education, Nanjing Normal University, Nanjing 210023, China (e-mail: jingxuanzhu@njnu.edu.cn; q.dai@njnu.edu.cn; xiaoyuanyuan_nnu@njnu.edu.cn; jun.zhang@njnu.edu.cn).

Lu Zhuo is with School of Earth and Environmental Sciences, Cardiff University, Cardiff CF10 3AT, UK (ZhuoL@cardiff.ac.uk).

Dawei Han is with Department of Civil Engineering, University of Bristol, Bristol BS8 1TR, UK (d.han@bristol.ac.uk).

varying terrain, and it is unlikely that vertical observations of rainfall can be realized at continental or even global scales. The Tropical Rainfall Measuring Mission (TRMM) satellite launched in 1997 carried the first satellite-based Precipitation Radar (PR), which provided a homogeneous three-dimensional rainfall characterization dataset, making it possible to study the rainfall evolution patterns on a large-scale horizontally and vertically. Following this, the Global Precipitation Measurement (GPM) core satellite, an improved version of TRMM, was launched and started operation by NASA and JAXA in February 2014, carrying the first satellite-based Dual-frequency Precipitation Radar (DPR). The DPR is equipped with a second signal band (Ka-band) that operates at a higher frequency than the Ku-band, which is the only one available for the PR, and is designed to accurately capture light rainfall [25].

Several studies have utilized data from the PR to investigate various aspects of vertical precipitation. Petersen et al. [26] used TRMM data to study the vertical structure, lightning, and rainfall characteristics of Amazonian and South American convection, highlighting the comprehensive nature of the TRMM dataset. Haddad and Park [27] proposed a Bayesian approach to quantify vertical variability of rainfall using TRMM radar and microwave imager measurements. Additionally, recent studies have used GPM DPR to study rainfall microphysical characteristics such as DSD. For instance, Gorgucci and Baldini [28] evaluated the accuracy of DSD retrievals using DPR, emphasizing the need for vertical profiles that reflect natural variability. Sun et al. [29] used DPR data to study the developing, mature, and dissipating stages of tropical rainfall, and concluded that the ground-based DSD from DPR inversion is reliable. Ramadhan et al. [11] studied the vertical structure of raindrop size distribution over West Sumatera using GPM observations, providing insights into local rainfall patterns. Wen et al. [30] used DPR data to study the seasonal variations of vertical precipitation in East China below 16 km, and concluded that DPR observations can capture the details of precipitation features with high spatial resolution.

Although some studies have investigated the microphysical characteristics of vertical precipitation, there are still study gaps in rainfall energy estimation. Existing research on vertical precipitation characteristics also lacks in-depth analysis of pure liquid-phase precipitation studies. Most of the existing studies do not distinguish the phase state and focus on the formation process of precipitation at high altitude, ignoring the change rule of pure liquid precipitation at the near-surface, which precisely the key to rainfall energy estimates. The aim of this study is to propose a method for the vertical structural estimation of rainfall energy for the first time based on GPM DPR data, and to investigate the effect of season on its characteristics. This study contributes to accurately characterize surface rainfall energy and enhance rainfall evolution cognition through the retrieval of radar observation, which can help to improve the spatial interpolation study in areas with complex topography and large elevation variations, and to realize a more accurate estimation of soil erosion.

II. Study Area and Data

A. Study area

The UK has a latitudinal range of approximately 49°N to 59°N. Its climate is temperate maritime, influenced by the North Atlantic Warm Current. This climate is characterized by frequent rainfall in winter and autumn, with high and uniform annual precipitation. According to the State of the UK Climate 2022 [31], the climate in the UK is becoming increasingly wet. Over the past decade, the annual rainfall has increased by 8% compared to the period from 1961 to 1990. Notably, 2014 and 2020 have ranked among the top 10 wettest years in UK history. In addition, the recent annual rainfall is likely influenced significantly by extreme years. Thunderstorms and torrential downpours have become more frequent, exacerbating intermittent flooding problems [31].

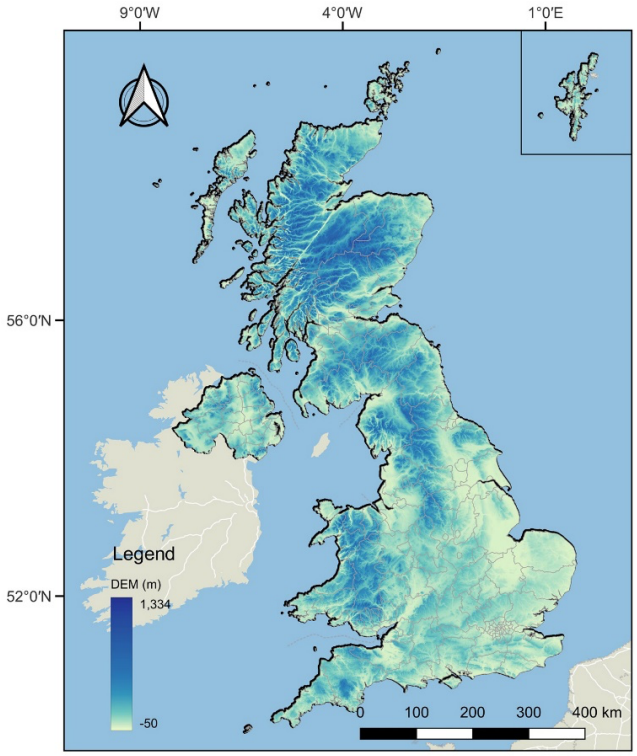

Fig. 1. DEM map in the study area.

B. GPM DPR data

The GPM DPR became operational in April 2014. It represents the first dual-frequency precipitation radar in the world, incorporating both Ku (13.6 GHz) and Ka (35.5 GHz) bands with swath widths of 245 and 120 km, respectively. The footprint resolution is 5 km with a vertical resolution of 125m. DPR enables all-weather precipitation observations over land and ocean, representing a significant enhancement over its predecessor, TRMM PR. The primary objectives of DPR include enhancing the accuracy and sensitivity of precipitation detection and providing global three-dimensional microphysical precipitation characteristics (e.g. shapes and sizes) to lead a better understanding of storms. The Ka-band portion of DPR, known as KaPR, primarily detects echoes from ice and snow particles, typically used for detecting snowfall and

weak precipitation events. Meanwhile, the Ku-band portion, known as KuPR, effectively captures echoes from intense precipitation events, primarily used for detecting heavy rainfall. By obtaining differentiated information from the two bands simultaneously, the three-dimensional precipitation particle size distribution can be achieved.

This study uses Full scan Swath (FS) data from GPM Level-2 DPR product (2ADPR) version 7, covering the period of January 2015 to December 2022 across the entire UK. The research focuses on precipitation observations with a liquid-phase state in the range of 0~6 km above sea level and examines two major rainfall types: stratiform and convective. Fig. 2 shows the probability density function (PDF) of the number of rainfall records for whole altitude data and surface data in the study area over the eight-year period. Each bar represents a 125 m vertical bin. Fig. 2(a) shows that most rainfall occurs below 4 km altitude, with the highest rainfall concentration in the 500~625 m bin. Convective rainfall is more common at altitudes below 750 m and above 3000 m, compared to stratiform rainfall. Fig. 2(b) illustrates the record amount at the surface level, indicating a higher PDF for convective rainfall within the 0~125 m bin and a higher PDF for stratiform rainfall within the 125~250 m bin. The PDF differences between the two rainfall types are less apparent in other bins. The yellow dashed line in Fig. 2(b) represents the elevation PDF of the land surface at a grid scale (0.1°×0.1°), which exceeds the PDF of both rainfall types within the 125~375 m range, suggesting a higher frequency of surface rainfall below 125 m elevation. To better understand the vertical profiles, two rainfall scanning cases, January 9, 2020 at 0:46:17 UTC (Case A) and February 15, 2020 at 13:43:22 UTC (Case B), were selected for case study (Table I).

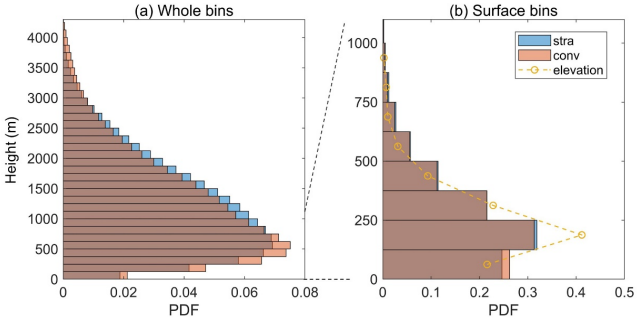

Fig. 2. Probability density function (PDF) of the rainfall record number for whole height data (a) and surface data (b) in the study area between 2015 to 2022. The yellow dashed line in (b) represents the land surface elevation PDF at the 0.1°×0.1°grid scale.

TABLE I
THE BASIC INFORMATION FOR STUDY DATE AND THE TWO SCANNING CASES

	Start Time	End Time	Stratiform pixel number	Convective pixel number
Whole period	2015-01-01 08:30:26 UTC	2022-12-31 18:46:37 UTC	13,380,356	946,213
Case A	2020-01-09 0:46:17 UTC	2020-01-09 0:48:56 UTC	2,194	220
Case B	2020-02-15 13:43:22 UTC	2020-02-15 13:46:06 UTC	2,357	188

III. METHODOLOGY

A. DSD function algorithm

DSD function is essential in characterizing precipitation microphysics and is commonly expressed in the three-parameter gamma distribution form [9], [16], [32]. It defines the number of particles in the unit volumn for each unit diameter (D) interval, denoted as $N(D)$:

$$N(D) = N_w f(\mu)\left(\frac{D}{D_m}\right)^{\mu} \exp\left[-\frac{(4+\mu)D}{D_m}\right] \quad (1)$$

$$f(\mu) = \frac{6(4+\mu)^{\mu+4}}{4^4\Gamma(\mu+4)} \quad (2)$$

where $f(\mu)$ is a function of the shape parameter μ, Γ represents the gamma mathematical function, N_w ($\mathrm{mm^{-1}\cdot m^{-3}}$) is the normalised intercept parameter, and D_m (mm) is the mass-weighted diameter parameter, defined as:

$$D_m = \frac{\int D^4 N(D) dD}{\int D^3 N(D) dD} \quad (3)$$

In the DPR algorithm, μ is constant and assumed to be 3. It then applies two types of I (rainfall intensity)–D_m relationships to estimate DSD parameters for stratiform [Eq (7)] and convective rain [Eq (8)], respectively.

$$I = 0.401\varepsilon^{4.649} D_m^{\ 6.131} \quad \text{(for stratiform)} \quad (4)$$

$$I = 1.370\varepsilon^{4.258} D_m^{\ 5.420} \quad \text{(for convective)} \quad (5)$$

In the retrieval process from the storm top to the actual surface, ε serves as an adjustment factor, remaining constant throughout. Once ε is established, the effective radar reflectivity factor (Z_e) values are utilized to search for I and D_m in the scattering tables for each range bin. Due to the different scan swaths of the KuPR and KaPR, the DPR FS data comprises High sensitivity beam scan Swath (HS) data collected from the inner swath where both Ku and Ka bands are scanned simultaneously, as well as other observations obtained solely from the outer swath where only Ku band is scanned. These data are processed separately using dual-frequency and single-frequency algorithms for estimation. In the dual-frequency algorithm, ε can be inferred when Ku-Z_e and Ka-Z_e bands are available. Conversely, in the single-frequency algorithm, the determination of ε relies on the monthly DSD database at grid scale to align its estimation closer to the results obtained from the dual-frequency algorithm. After determining I and D_m, N_w can be solved according to the following equation:

$$I = 6\pi \times 10^{-4} \int N(D) D^3 V(D) dD \quad (6)$$

B. DPR-based rainfall energy estimation

According to the kinetic energy formula, the energy of a raindrop (e, unit: J) is determined by its mass m (kg) and the velocity v ($\mathrm{m\ s^{-1}}$). Assuming the raindrop is spherical, ej can be calculated using the diameter D (mm):

$$e = \frac{1}{2} m v^2 = \frac{\pi}{12} 10^{-6} \rho v^2 D^3 \tag{7}$$

where ρ is the density of water (1 g cm^{-3}). Due to air resistance, the terminal velocity of raindrops near the ground remains constant. The following *V–D* relationship is used to estimate *v* [33]:

$$v(D) = [9.65 - 10.3\exp(-0.6D)]\left(\frac{\rho_0}{\rho_a}\right)^{0.4} \tag{8}$$

where ρ_0 (1.20 kg m^{-3}) and ρ_a are the air densities at sea level and observation altitude, respectively.

The sum of the kinetic energy of each rain drop, within a given rain depth that hits a given area, defines the total kinetic energy. The rainfall kinetic energy KE_t for the unit time (J m^{-2} h^{-1}) can be calculated as the product of the kinetic energy of each drop of each diameter class, which can be expressed as follows:

$$KE_t = 3600 e_{sum} = 3600 \frac{\pi\rho}{12} 10^{-6} \int N(D) v^3 D^3 dD \tag{9}$$

where e_{sum} (J m^{-2}) is the total energy of all raindrops per unit area (m^2).

C. Phase and rain type division algorithms

The DPR relies on the Classification (CSF) module to categorize precipitation pixels into three types: convective, stratiform, and other. As stratiform precipitation is characterized by low intensity, widespread coverage, and often accompanied by bright band echoes, the bright band (BB) is widely utilized for identifying stratiform precipitation. For the single-frequency module, DPR utilizes the V-method (vertical profiling method) and H-method (horizontal pattern method) in conjunction to determine precipitation types [25]. The V-method initially identifies the presence of a bright band on the vertical profile and then assesses whether the reflectivity factor meets the typical conditions for different rain types. For instance, if BB is detected, and the reflectivity factor does not exceed 46 dBZ (known as special convective threshold), it is classified as stratiform type; if BB is not detected, and the reflectivity factor exceeds 40 dBZ (known as conventional convective threshold), it is classified as convective type [25], [34]. The H-method utilizes the University of Washington convective/stratiform separation method [35] to determine if the maximum reflectance coefficient in the horizontal pattern of the radar beam exhibits convective characteristics. If it is not of the convective type, the magnitude of the reflectivity is then used to determine if the precipitation is stratiform rain, otherwise it is classified as "other". In the dual-frequency algorithm, precipitation is classified using the measured dual-frequency ratio (DFR_m) method [23], which utilizes the difference between the reflectivity (in dB units) of Ku and Ka bands. The method involves identifying points of local maximum and minimum values of DFR_m, which are key in classifying the precipitation type. The empirical parameters C_1 (0.18) and C_2 (0.20) are used in the decision rule:

$$V_1 = \frac{DFR_{ml}(\max) - DFR_{ml}(\min)}{DFR_{ml}(\max) + DFR_{ml}(\min)} \times 100\% \tag{10}$$

$$V_2 = \mathrm{abs}(\mathrm{mean}(DFR_m slope)) \tag{11}$$

$$type = \begin{cases} stratiform, \dfrac{V_1}{V_2} > C_2 \\ other, C_1 \le \dfrac{V_1}{V_2} \le C_2 \\ convective, \dfrac{V_1}{V_2} < C_1 \end{cases} \tag{12}$$

In the algorithm for phase state identification in DPR, for precipitation with a BB, five bins are selected from the storm top bin to the land surface bin, naming them as nodes A to E from top to bottom [25]. Among them, B and D represent the upper and lower boundaries of the BB, respectively, while A and E represent bins where the particle temperature is closest to -20°C and 20°C, respectively. Node C corresponds to the peak of the BB. In cases without a BB, nodes B, C, and D are all considered to be located at the 0°C range bin. Above node A, the particle phase state is solid, while between nodes A and D, it is classified as mixed phase state. This study focuses on liquid precipitation, specifically rain particles located below node D.

D. Evaluation method

To understand the vertical variation of variables, the change rate *R* can be calculated using the difference in variable values between adjacent height layers in the same observation column. When the variable is absent in the preceding height bin, it is excluded from the calculation. The equation is defined as follows:

$$R_i = \frac{X_i - Y_i}{Y_i} \times 100\% \tag{13}$$

where X_i and Y_i refer to the observed values in the lower and upper bins of the i^{th} sample pair, respectively.

In addition, in order to assess the correlation of variables of neighboring height bins, Pearson's correlation coefficient is used in this paper, defined as:

$$Pearson = \frac{\sum (X_i - \overline{X})(Y_i - \overline{Y})}{\sqrt{\sum (X_i - \overline{X})^2} \sqrt{\sum (Y_i - \overline{Y})^2}} \tag{14}$$

IV. RESULTS

A. DPR DSD parameters and intensity distribution

The scanning scenarios for both at 500 m altitude are represented in Fig. 3 (a~d) and (e~h), respectively. The events used for the vertical analysis examples are marked with horizontal lines in Fig. 3 (a) and (e). There are four variables in Fig. 3, including rainfall type, D_m, N_w in logarithmic form with base 10 (lgN_w) and *I*, where the first three variables are obtained from the 2ADPR product and *I* is calculated from D_m and N_w. Both selected cases contain two distinct types of rain, stratiform rain and convective rain, divided in DPR CSF module.

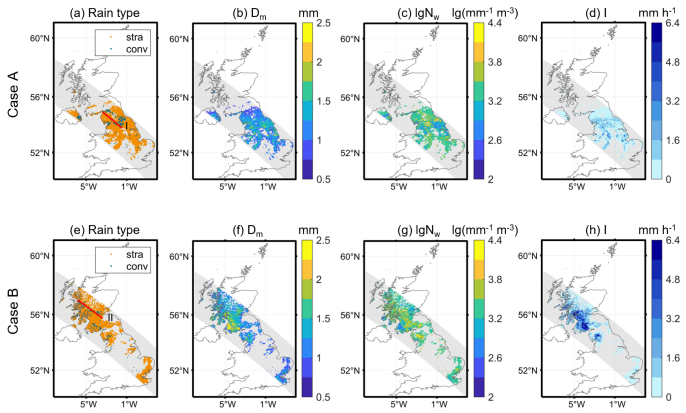

Fig. 3. Scanned Cases A and B of DPR-derived rain type (a, e), D_m (b, f), lgN_w (c, g) and I (d, h) at 500 m.

Specifically, in Case A, the DPR observed widespread rainfall in the north of England and the east of Northern Ireland, with I concentrating on less than 3 mm h^{-1}, D_m concentrating on less than 1.5 mm, and lgN_w mainly distributing between 2.8 and 3.7. In Case B, the DPR primarily scanned rainfall over western and southern Scotland, and observed small-scale rainfall over eastern England. Two main rainfall centers are identified, one in the range from the western side of the Southern Uplands to the southwestern part of the Grampian Mountains, and the other at Scafell Pike. The I of Case B is significantly higher than I scanned in Case A. Meanwhile, most rainfall in the western region of the Southern Uplands exceeded 4 mm h^{-1}, resulting in raindrop sizes that were generally higher than in case A. Here, D_m values are mainly above 1 mm, with high values exceeding 2.5 mm and appearing in bright yellow in Fig. 3(f), and lgN_w values are similar to those of Case A, also concentrated around 3.5.

Fig. 4 shows the vertical profile distribution of variables for Event I and II (labeled by the red lines in Figs. 3(a) and (e), respectively). The black lines at the bottom of subfigures represent the ground elevation values. Below the black line, there is no rainfall observation data in DPR data, so it is shown as a white color patch under the black line. The symbol "×" indicates that the rainfall type of the column is convective rainfall, while the absence of the symbol "×" indicates stratiform rainfall. In Fig. 4(a~c), the liquid observation heights for Event I basically do not exceed 1000 m above sea level. Among them, I values are concentrated in the range below 1.5 mm h^{-1}, and the vertical variations of D_m, lgN_w and I on the same column are almost invisible. For Event II, the overall rainfall intensity is much higher than Event I, and the liquid precipitation height top is also higher. This is mainly due to the high values of D_m, which are mostly above 1.5 mm. Vertical variations of several column variables can be clearly seen in the figure, where D_m tends to decrease from the top to the bottom, and the corresponding I also tends to decrease despite the increase of some of the lgN_w values. In addition, the lgN_w of the convective rain in the two events is significantly higher than that of the stratiform rain type, which corresponds to lower D_m values.

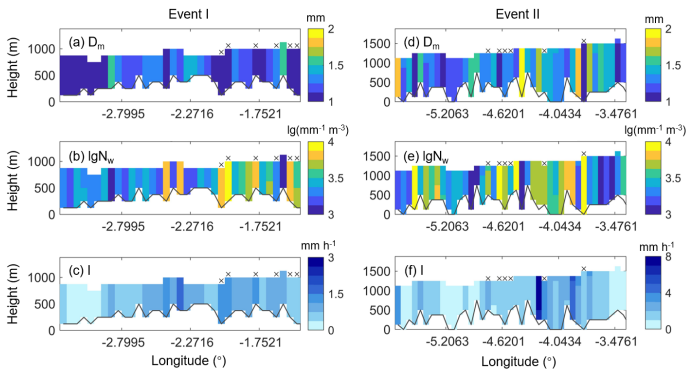

Fig. 4. Vertical profile of D_m (a, d), lgN_w (b, e) and I (c, f) in Events I and II. Note that black dash lines at the bottom of subfigures represent the surface altitude, and the "×" is labeled for convective rain.

Fig. 5 illustrates the contoured frequency of variables versus observed heights for different rainfall types over the eight years, and due to the magnitude differences, the quantities were logarithmized before calculating the frequencies. Here, Fig. 5(a~c) are for stratiform rain and (d~f) are for convective rain. In this study, liquid precipitation within 6 km was selected for analysis, and it can be seen from the figure that there is very little liquid precipitation over 4 km, and most of the liquid precipitation is concentrated below 2 km, regardless of the type of rainfall. Comparing Fig. 5(a) and (d), the density centers of D_m for stratiform rain are higher than those for convective rain, which are 1 mm and 0.85 mm, respectively, and the low D_m contours for convective rain are more compact, suggesting that the D_m size is more concentrated in this case. Meanwhile, lgN_w in Fig. 5(b) and (e) show opposite characteristics, with higher values of convective rain centered around 3.7 and stratiform rain at 3.3. In addition, in Fig. 5(f), the density of convective rain does not maintain a decreasing trend with the increase in intensity after it is larger than the center of density (about 0.23 mm h^{-1}). Instead, a second center of density occurs near 1.72 mm h^{-1}, and the altitude ranges of frequencies in the range of 50~78 lg% (between yellow and orange patches) continue to expand with the increase in rainfall intensity even between the two centers of density. It is noteworthy that the DSD parameter contours in the middle layer in Fig. 5(d) and (e) both have a small tail, indicating that the number of raindrops in convective rain is much larger at lower elevations than at higher elevations. This result may be attributed to the fact that the strong updrafts present in convective rains provide great opportunities for the growth of raindrops of varying diameters beneath the cloud base. Consequently, this phenomenon leads to an increased number of raindrops (large N_w values) and a broad range of intensities at lower altitudes.

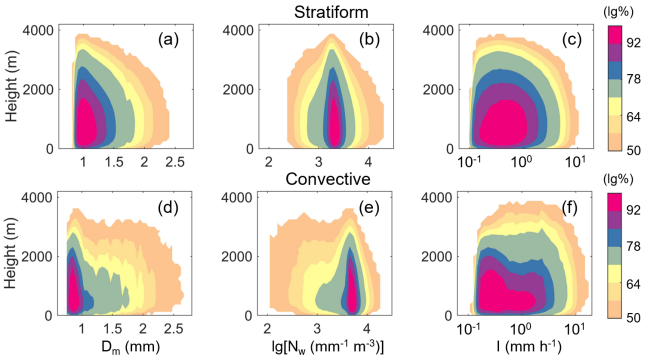

Fig. 5. Contoured frequency of D_m (a, d), lgN_w (b, e) and I (c, f) versus observed heights for stratiform (a~c) and convective (d~e) rain in 2015~2022.

B. Change ratio of DSD parameters and intensity

In this study, the R of D_m, lgN_w, and I are defined as R_D, $R_{\lg N}$ and R_I, respectively. Positive values of the R represent an increase change in current bin compared to the upper bin, while negative values represent the opposite. Fig. 6 shows the vertical profiles of R_D, $R_{\lg N}$ and R_I for Event I and II. It can be seen that the R_D ratios do not vary much and are mostly negative in the vertical view, indicating that the D_m in the air is basically unchanged from top to bottom, with a tendency for individual precipitation columns to decrease. Specifically, the liquid precipitation columns for Event I show little vertical variation in D_m, while Event II shows more columns with variations in D_m, which may be due to more intense rainfall. As for lgN_w, it can be seen from Figs. 6(b) and (e) that all columns for both events change and show a continuous upward trend from top to bottom, except for the tops of individual rain columns of Event II appear to have negative values of $R_{\lg N}$.

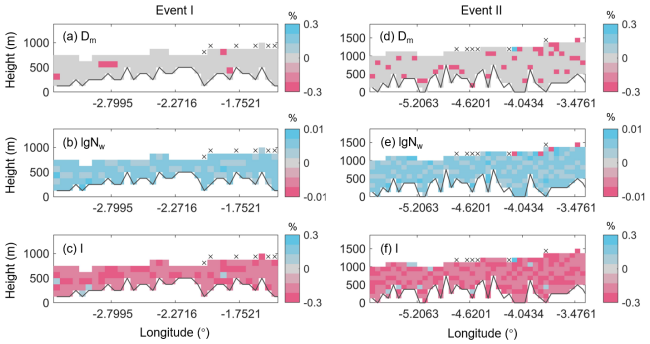

Fig. 6. Vertical profile of R_D (a, d), $R_{\lg N}$ (b, e) and R_I (c, f) in Events I and II. Note that black dash lines at the bottom of subfigures represent the surface altitude, and the "×" is labeled for convective rain.

However, from the top to the bottom, under the situation of almost constant D_m and increasing lgN_w, the overall trend of I decreases, mainly due to the increase of air pressure with decreasing altitude, which reduces the raindrop velocity, while the DSD does not change or changes very little, which further affects the gradual decrease of I. Nevertheless, there are still some records with positive R_I, suggesting that the effect of DSD changes on I exceeds the suppression of I increase by altitude decrease at this time.

Fig. 7 depicts the contoured frequency distribution of R_D, $R_{\lg N}$ and R_I with height for eight years of stratiform and convective rain. All frequency plots show a tree structure. From the bottom to the top, at heights below about 750 m, the majority of the RI is concentrated near the value of 0, which looks like a tree trunk in the diagram. Above 750 m, it looks like a canopy, where the R range increases dramatically at an altitude bin of 875 m, and reaches its maximum range near 1500 m altitude. Further up it decreases and forms a tree top at 3000 m in the figure.

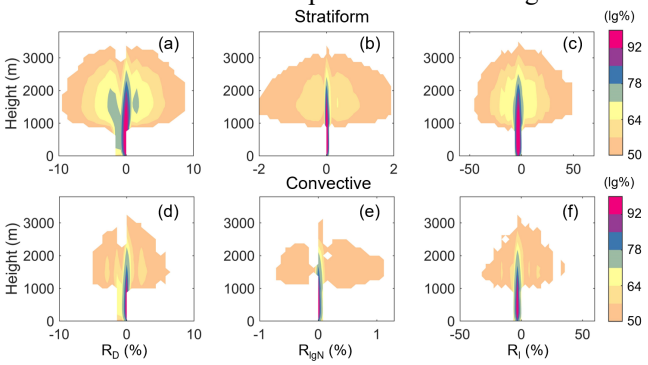

Fig. 7. Contoured frequency of R_D (a, d), $R_{\lg N}$ (b, e) and R_I (c, f) versus observed heights for stratiform (a~c) and convective (d~e) rain in 2015~2022.

From the height-concentrated purple patches in the figure, the high frequency R are all concentrated near the 0 value. Considering 750 m as the demarcation between high and low altitude, the R_D and R_I in the figure are all lower than 0 while $R_{\lg N}$ is all higher than 0 at low altitude, which indicates that most of the raindrop diameters decrease with decreasing altitude, accompanied by a gradual increase in the concentration of the raindrops. And the R values at high altitude take a wider range of values, reflecting a series of complex microphysical characteristic changes of raindrops in the high air. Among the three variables, $R_{\lg N}$ is clearly the one with the largest difference between high and low altitudes. In terms of rain types, stratiform rain has a wider range of R values than convective rain, and the "canopy" is more luxuriant. The orange ranges of R_D and $R_{\lg N}$ for the stratiform rain in the figure are about more than twice as wide as for the convective rain. The differences in vertical distribution of raindrop parameters between stratiform and convective rain may be attributed to the distinct dynamics within these rain types. In stratiform rain, the weak vertical motion results in stable changes in water content and temperature with altitude, leading to less variability in DSD. However, external factors like terrain uplift can disrupt this stability, altering the coalescence process of raindrops. In contrast, convective rain features strong updrafts that promote a uniform vertical DSD due to vigorous mixing, despite the intense convective activity.

C. KE_t and R_{KE} distribution

Fig. 8 shows the track distribution of KE_t calculations for the two cases at a height of 500 m above sea level. It can be seen that most of the KE_t in the scanning range of Case A does not exceed 20 J m^{-2} h^{-1}, while Case B has a large area of KE_t exceeding 60 J m^{-2} h^{-1} in the high-intensity rainfall region in the western part of the Southern Highlands, showing a decreasing

trend of KE_t from the southwestern part of Scotland to the central part of the country. The vertical variability of KE_t in Fig. 9 (a) and (b) is more obvious compared to the vertical profiles of DSD parameters and I in both Events in Fig. 4. For the R_{KE} profiles in Fig. 9 (c) and (d), the distribution characteristics are similar to the R_I but the pattern of decreasing with height is more apparent. However, compared to the presence of more than ten positive values in the R_I profiles in both Events, the corresponding R_{KE} values are almost all negative.

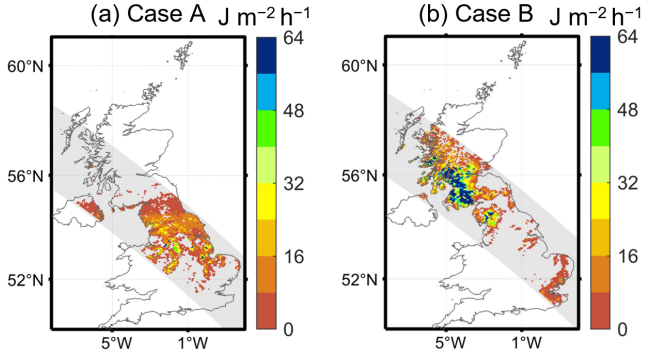

Fig. 8. Scanned Cases A and B of DPR-derived KE_t at 500 m.

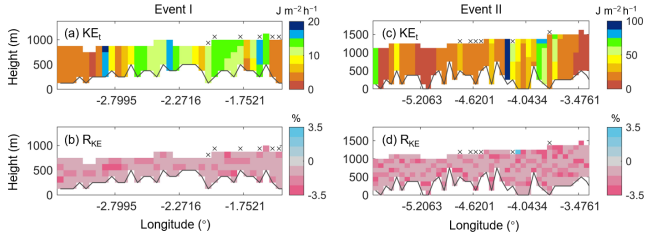

Fig. 9. Vertical profile of KE_t (a, c), R_{KE} (b, d) in Events I and II. Note that black dash lines at the bottom of subfigures represent the surface altitude, and the "×" is labeled for convective rain.

Fig. 10 shows the contoured vertical frequencies of KE_t and R_{KE}. The range of KE_t values for convective rain is almost twice as large as that for stratiform rain, with the outermost contours reaching a maximum of more than 400 and 200 J m^{-2} h^{-1}, respectively. From the high-density patches (in rosy red) in the figure, it appears that more convective rain occurs at low heights and has a wider range of KE_t values compared to high heights, with a second density center near 10 J m^{-2} h^{-1}. In addition, high-energy convective rain is even more distributed at high altitudes above 3000 m than low-energy rainfall at the same height, reflecting the complexity of the raindrop dynamics within the convective rain. The frequency change of stratiform rain, on the other hand, is very smooth, with the frequency decreasing from the center of the distribution around 5 J m^{-2} h^{-1} outward. For R_{KE}, both rain types take values below 0 at low altitudes, with a large number of records mainly clustered around -5%, indicating that the R_{KE} tends to decrease from top to bottom at low altitudes, and the magnitude is large. Similarly, the outermost contour of R_{KE} for stratiform rain is much more than that for convective rain, indicating that the vertical R_{KE} of convective rain is also more concentrated with a higher value of R_{KE}, indicating that convective rain is relatively maintained at a higher energy level.

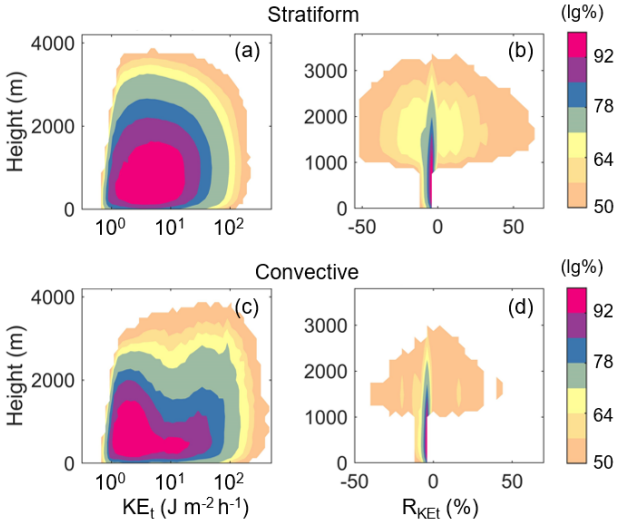

Fig. 10. Contoured frequency of KE_t (a, c), R_{KE} (b, d) versus observed heights for stratiform (a, b) and convective (c, d) rain in 2015~2022.

Fig. 11 and 12 show the gridded distribution of the mean values in KE_t and R_{KE} for the eight-year observations of the two rainfall types in each 250 m height interval for observation heights from 250 to 1500 m, respectively, with a gridded resolution of 0.1°. The maximum plotting height of 1500 m was chosen because the UK does not exceed 1500 m. It can be seen from Fig. 11 that the overall values of KE_t take an upward trend with the observed height, regardless of the rain type. Meanwhile, the KE_t of convective rain is much higher than that of stratiform rain at the same height in the same region. The KE_t of stratiform rain is highest in the coastal areas of western and southern England and central England on average, and the high KE_t of convective rain is more concentrated in all of England. This suggests that convective rain energy is lower in mountainous regions (e.g. the Scottish Highlands) than in other terrains, and is also related to the characterization of convective rain as seen in Fig. 10 (c) as occurring mostly at low altitudes.

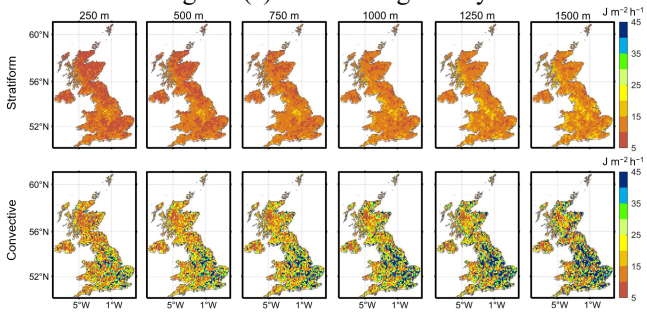

Fig. 11. Spatial distribution of mean KE_t for stratiform and convective rain at various heights.

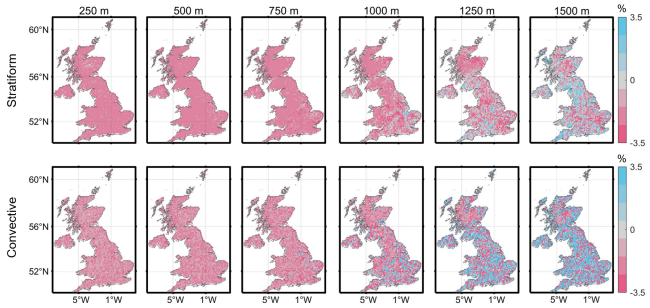

Fig. 12. Spatial distribution of mean R_{KE} for stratiform and convective rain.

As can be seen in Fig. 12, the same rain type R_{KE} values from 250~750 m are not much different and are mostly negative. As the height increases, more and more positive values appear, and up to 1500 m, the positive and negative values are almost split in half. In addition, for R_{KE} at the same height, the mean value of R_{KE} of stratiform rain is always lower than that of convective rain, which is shown by the fact that the absolute value of R_{KE} of stratiform rain is larger when both R_{KE} values are negative, and the R_{KE} of stratiform rain is smaller or negative when convective rain R_{KE} is positive. This shows that the R_{KE} of stratiform rain decreases more rapidly from top to bottom at low observation altitudes, while the R_{KE} of stratiform rain increases more slowly from top to bottom at high heights.

D. Season variability of KE_t and R_{KE}

To comprehend the influence of season on KE_t and R_{KE}, Fig. 13 illustrates the mean curves and lower to upper interquartile ranges of distinct rainfall types for all (black solid curve) and for the different seasons (color solid curve) using shade error plots, as derived from the records between 2015 and 2022. Here, March~May, June~August, September~November, and December~February are regarded as spring, summer, fall, and winter, respectively. In general, there is little seasonal variation at lower altitudes, the mean KE_t values in stratiform rain were 8.74, 12.24, 12.00, and 9.01 J m^{-2} h^{-1} in the four seasons at altitudes below 1500 m. In contrast, the mean KE_t values in convective rain were 19.22, 27.07, 18.50, and 15.91 J m^{-2} h^{-1}, exhibiting higher values than those observed in stratiform rain. However, a large seasonal variation occurs above 1500 m, although the KE_t curves for the overall feature (black curve) and for summer (red curve) almost overlap. In summer, the mean KE_t reaches maximum among the four seasons for almost all heights for both rain types, with only convective rains between 2000 and 3000 m are exceeded by spring (green curve). In addition, mean KE_t was lowest in winter at most altitudes, and lowest in spring for stratiform rain between 1000 and 2000 m and 3250 and 3750 m. Seasonal differences in rainfall energy are subtle at lower altitudes, but as altitude increases, the mean value curve (black) approaches the summer season curve (orange), likely due to variations in liquid water height across seasons. Higher temperatures in summer correspond to greater rainfall heights, with autumn and spring following, and winter having the lowest. Additionally, the high number of thunderstorms in the UK during summer leads to the highest convective rainfall energy near the surface for all seasons

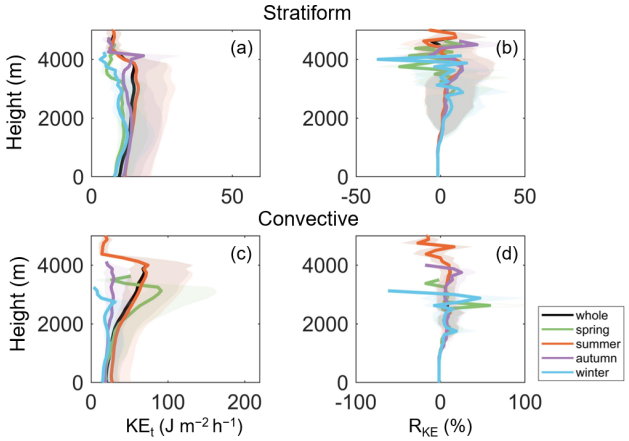

Fig. 13. Shade error plot of KE_t (a, c) and R_{KE} (b, d) for stratiform and convective rainfall.

In Fig. 13(b) and (d), all R_{KE} curves for distinct seasons and both rain types exhibit negative values at low altitudes (below 1125 m for stratiform rain and below 1625 m for convective rain). The minimum values of the R_{KE} curves are observed at the lowest latitudes, with an overall value of approximately -1. 68%. The R_{KE} values all increase progressively with height, and the convective rain takes on a wide range of fluctuations earlier than the stratiform rain, reappearing near 2500 m with negative values, while stratiform rain manifests around 3000 m. Similarly, the black curve overlaps almost exactly with the orange solid line representing summer. The winter months of stratiform and convective rain show a very large fluctuation and then disappear near 4000 and 3125 m at high altitudes, respectively. The next most pronounced fluctuation in R_{KE} values is in spring. The pronounced R_{KE} variations in both seasons may be related to the small base of KE_t itself.

Figs. 14 and 15 show the spatial distribution of seasonal mean KE_t and R_{KE} on the 0.1° grid, respectively, at three altitudes (500, 1000, 1500 m) selected for analysis. In Fig. 14, the highest overall KE_t values are observed in summer, followed by autumn. The areas of high KE_t values in summer are concentrated throughout England, while the areas of high values in spring, autumn and winter are located in southern England, central England and southern Scotland, respectively. The KE_t values increased substantially with increasing height in all seasons, with the most pronounced increase in the west of Scotland during winter, whereas there was little spatial variation across the country at 1500 m height in fall, with the high values mainly located in the coastal regions of England and Scotland across the whole UK. Whereas the seasonal differences in R_{KE} are not obvious in Fig. 15, the brighter colors of the R_{KE} distributions in spring and winter at 1500 m height indicate that the absolute values of R_{KE} are larger and KE_t varies significantly at this height.

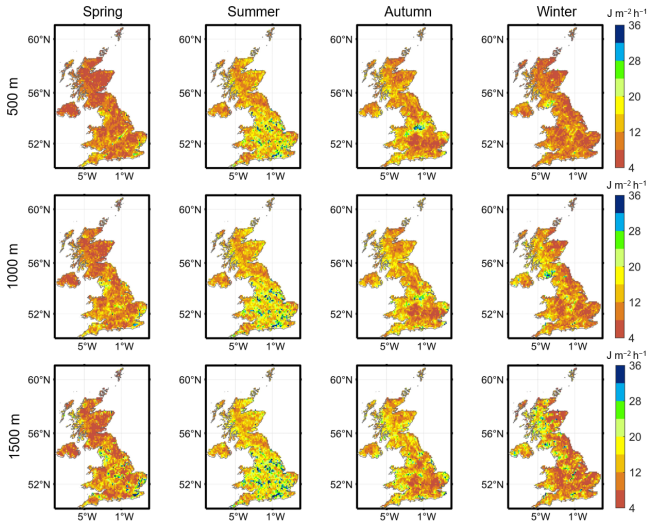

Fig. 14. Spatial distribution of mean KE_t at 500, 1000, 1500 m, respectively.

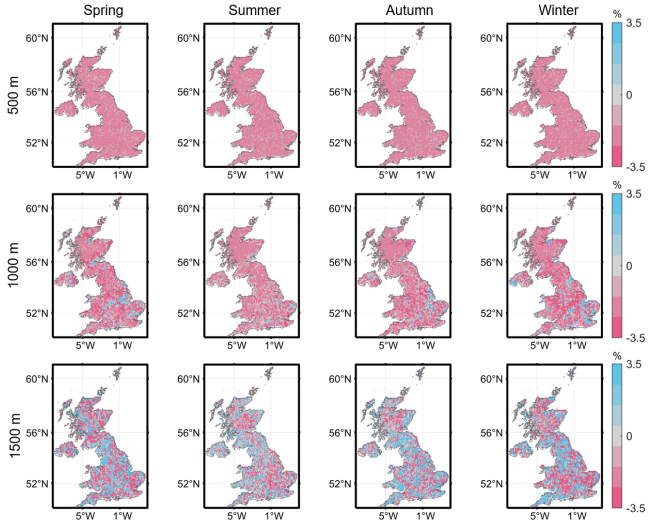

Fig. 15. Spatial distribution of and mean R_{KE} at 500, 1000, 1500 m, respectively.

E. Comparison of rainfall characteristics at different heights

Table II compares the correlation of rainfall microphysical parameters between two neighboring height bins below 1500 m using the Pearson coefficient. It can be seen that the same parameter has an extremely strong correlation vertically, with all values exceeding 0.99. Regarding the type of rainfall, stratiform rain always has a higher correlation than convective rain. D_m is the highest correlation among the parameters, with Pearson values of 0.9988 and 0.9967 for stratiform and convective rain, respectively. The second highest for stratiform rain is still the DSD parameter, lgN_w, as high as 0.9981, but its correlation in convective rain is the worst among the four variables at 0.9946. In addition, Pearson of I is slightly higher than that of KE_t in both rain types, and the difference between rain types is smaller than that of DSD parameters, neither exceeding 0.002.

TABLE II

PEARSON FOR NEIGHBORING HEIGHT BINS BELOW 1500 M.

	D_m	lgN_w	I	KE_t
Stratiform	0.9988	0.9981	0.9974	0.9973
Convective	0.9967	0.9946	0.9966	0.9957

Table III shows the mean and standard deviation of the R values within 1500 m. It is found that the R means are always negative during stratiform rain, except for lgN_w. During convective rainfall, only the R mean values of D_m and KE_t are negative, and the mean value of R_D is close to 0. In addition, the R means of DSD parameters are small, and none of them exceeds 0.1% in absolute value. In contrast, the absolute values of the means of R_{KE} are very large, all exceeding 0.5%, and even as high as 1.35% for stratiform rain, indicating that the degree of variability of KE_t is more dispersed than the other variables within the 1500 m height. Similarly, the standard deviation of R_{KE} always takes the largest value among the four variables regardless of the rain type. The high standard deviations of R_I and R_{KE} for convective rain also indicate that the vertical characteristics of convective rain exhibit a high degree of dispersion.

TABLE III

THE AVERAGE VALUE AND STANDARD DEVIATION OF R WITHIN 1500 M.

	Average			
	D_m	lgN_w	I	KE_t
Stratiform	-0.08	0.08	-0.20	-1.36
Convective	-0.01	0.08	0.34	-0.64
	Standard deviation			
	D_m	lgN_w	I	KE_t
Stratiform	1.57	0.72	8.52	12.08
Convective	1.70	0.80	15.45	28.37

V. DISCUSSION

The GPM DPR observations provide valuable insights into rainfall characterization, but uncertainties remain. These uncertainties arise from limitations in the accuracy of DPR observations and the attenuation of the signal during observations from heights of hundreds of kilometers to the ground, resulting in potential errors in the observations [36]. DPR V06 was also subject to uncertainty introduced by ground clutter, which biased the estimates from the true values at the surface below 1 km (especially in complex terrain such as mountains) [37]. In V07, the DPR algorithm has been significantly improved in terms of clutter handling, and an improved side-lobe clutter removal procedure has been implemented based on [38], which greatly mitigates the effects of residual clutter signals. Currently, the validation of DPR rainfall characterization observations relies heavily on ground-based instruments, supplemented by GPM own ground-based validation network. However, there are still gaps in research on the accuracy of satellite rainfall microphysical observations, highlighting the need for further validation using tools such as wind profiler radar. However, despite these uncertainties, DPR can be a valuable tool for analyzing rainfall microphysical horizontal and vertical spatial characteristics.

Additionally, DPR utilizes a fixed μ of 3 in its gamma distribution model for DSD, which is a simplification that

introduces some uncertainty into the rainfall estimates. For instance, disdrometer data from various geographical regions show that while the mode of μ corresponds to the DPR fixed value ($\mu = 3$), the median is higher ($\mu = 7$), indicating substantial natural variability in μ [39]. However, studies suggest that the impact of this practical choice is relatively minor and within acceptable operational limits [40], [41]. While this discrepancy adds to DSD estimation uncertainty, it does not significantly impair the precipitation estimates in DPR. Research indicates that retrieval errors from fixed-μ relations are small, with biases typically less than +/- 10%, suggesting that the effect of the fixed μ is not substantial enough to invalidate the DPR data [41]. The operational requirements of the DPR necessitate a balance between precision and practicality, and the current setting strikes a balance that allows for effective large-scale precipitation monitoring [41].

Whilst our study makes a significant contribution to understanding the vertical variability of rainfall microphysics in the UK, it is important to recognize the limitations of DPR observations. Due to the orbital nature of the DPR on the satellite, rainfall observations at the same location are discontinuous. Therefore, DPR alone cannot capture the complete evolution of a storm system in a given region. Future research efforts will aim to address this limitation by integrating data from disdrometers at different altitudes, as well as observations from radar systems and numerical weather prediction models capable of observing at high altitudes. This integrated approach will help to develop more accurate three-dimensional rainfall energy datasets that provide a comprehensive understanding of rainfall dynamics and its vertical variability.

VI. Conclusions

This study is the first to analyze the vertical profile characteristics of KE_t using the GPM DPR. The study explores the vertical variations in rainfall microphysics and energy over the UK using data from the DPR in eight years (2015~2022). This work introduces the variable R between height bins to amplify the vertical spatial variations of rainfall, enabling investigation into the representativeness of ground-based observational instruments at different heights. The findings highlight significant spatial and temporal variations in rainfall microphysical characteristics and kinetic energy, overcomes the limitations of conventional instruments in estimating rainfall energy in three dimensions. Based on a series of analysis using eight-year DPR records, the following conclusions are concluded:

1. A strong correlation (over 0.99) between rainfall energy in adjacent 125 m height bins below 1500 m is found in UK. The correlation between KE_t in adjacent height bins is stronger in stratiform rain (0.9973) than in convective rain (0.9957), suggesting more variability in KE_t for the latter. Additionally, the DSD parameters (D_m and $\lg N_w$) exhibit higher vertical correlation and smaller standard deviation compared to I and KE_t.

2. At near-surface altitudes (below 1500 m), D_m, I and KE_t tends to decrease from top to bottom of the height, while $\lg N_w$ tends to increase. D_m shows less variation with height compared to $\lg N_w$, indicating more stable raindrop sizes at lower altitudes. Seasonal variations in KE_t are evident, with little variation at lower altitudes but notable differences above 1500 m. KE_t peaks in summer and reaches its lowest in winter, reflecting seasonal influences on rainfall energy distribution.

3. Convective rain typically shows larger raindrop sizes and higher intensity at lower altitudes, while stratiform rain shows more uniform microphysical characteristics, indicating different precipitation dynamics between rain types. Below 1500 m altitude, although the mean value of R_{KE} in stratiform rain is higher at 1.36% than in convective rain at 0.64%, the standard deviations are 12.08% and 28.37%, respectively, suggesting that stratiform rain is more variable at lower altitudes, but convective rain is more discrete in its variability. However, at altitudes above 3000 m, high-energy convective rainfall is more frequent than low-energy rainfall at the same altitude.

In conclusion, despite the limitations of DPR observations, they remain invaluable for analyzing rainfall characteristics, especially in terms of vertical variability. Our study emphasizes the importance of further validation efforts and integration of multiple observation platforms to improve the accuracy and completeness of rainfall datasets. By addressing these challenges, we can deepen our understanding of rainfall processes and improve the effectiveness of precipitation monitoring and forecasting systems.

References

[1] O. E. Adeyeri, P. Laux, A. E. Lawin, and J. Arnault, "Assessing the impact of human activities and rainfall variability on the river discharge of Komadugu-Yobe Basin, Lake Chad Area," *Environ Earth Sci*, vol. 79, no. 6, p. 143, Mar. 2020, doi: 10.1007/s12665-020-8875-y.

[2] T. Dinku, "The Value of Satellite Rainfall Estimates in Agriculture and Food Security," in *Satellite Precipitation Measurement: Volume 2*, V. Levizzani, C. Kidd, D. B. Kirschbaum, C. D. Kummerow, K. Nakamura, and F. J. Turk, Eds., Cham: Springer International Publishing, 2020, pp. 1113–1129. doi: 10.1007/978-3-030-35798-6_32.

[3] Intergovernmental Panel on Climate Change, *Climate Change 2021 – The Physical Science Basis: Working Group I Contribution to the Sixth Assessment Report of the Intergovernmental Panel on Climate Change*, 1st ed. Cambridge University Press, 2023. doi: 10.1017/9781009157896.

[4] N. K. Singh, R. E. Emanuel, B. L. McGlynn, and C. F. Miniat, "Soil Moisture Responses to Rainfall: Implications for Runoff Generation," *Water Resources Research*, vol. 57, no. 9, p. e2020WR028827, 2021, doi: 10.1029/2020WR028827.

[5] L. Zhuo, Q. Dai, B. Zhao, and D. Han, "Soil moisture sensor network design for hydrological applications," *Hydrology and Earth System Sciences*, vol. 24, no. 5, pp. 2577–2591, May 2020, doi: 10.5194/hess-24-2577-2020.

[6] A. F. Feldman *et al.*, "Plant responses to changing rainfall frequency and intensity," *Nature Reviews Earth and Environment*, vol. 5, pp. 276–294, Apr. 2024, doi: 10.1038/s43017-024-00534-0.

[7] L. Ni *et al.*, "Streamflow and rainfall forecasting by two long short-term memory-based models," *Journal of*

Hydrology, vol. 583, p. 124296, Apr. 2020, doi: 10.1016/j.jhydrol.2019.124296.
[8] Q. Dai, Q. Yang, D. Han, M. A. Rico-Ramirez, and S. Zhang, "Adjustment of radar-gauge rainfall discrepancy due to raindrop drift and evaporation using the weather research and forecasting model and dual-polarization radar," *Water Resources Research*, vol. 55, no. 11, Art. no. 11, 2019, doi: 10.1029/2019WR025517.
[9] Q. Dai and D. Han, "Exploration of discrepancy between radar and gauge rainfall estimates driven by wind fields," *Water Resources Research*, vol. 50, no. 11, Art. no. 11, 2014, doi: 10.1002/2014WR015794.
[10] Y. Zeng, L. Yang, Y. Zhou, Z. Tong, Y. Jiang, and P. Chen, "Characteristics of orographic raindrop size distribution in the Tianshan Mountains, China," *Atmospheric Research*, vol. 278, p. 106332, Nov. 2022, doi: 10.1016/j.atmosres.2022.106332.
[11] R. Ramadhan, Marzuki, and Harmadi, "Vertical structure of raindrop size distribution over West Sumatera from global precipitation measurement (GPM) observation," *J. Phys.: Conf. Ser.*, vol. 1876, no. 1, p. 012013, Apr. 2021, doi: 10.1088/1742-6596/1876/1/012013.
[12] R. Biswasharma *et al.*, "Sensitivity analysis of cumulus and microphysics schemes in the WRF model in simulating Extreme Rainfall Events over the hilly terrain of Nagaland," *Atmospheric Research*, vol. 304, p. 107393, 2024, doi: 10.1016/j.atmosres.2024.107393.
[13] G. Chen *et al.*, "Variability of microphysical characteristics in the '21·7' Henan extremely heavy rainfall event," *Sci. China Earth Sci.*, vol. 65, no. 10, pp. 1861–1878, Oct. 2022, doi: 10.1007/s11430-022-9972-9.
[14] Y. Shi *et al.*, "Investigation of vertical microphysical characteristics of precipitation under the action of low-frequency acoustic waves," *Atmospheric Research*, vol. 249, p. 105283, Feb. 2021, doi: 10.1016/j.atmosres.2020.105283.
[15] H.-J. Song and K.-S. Sunny Lim, "Evaluation of bulk microphysics parameterizations for simulating the vertical structure of heavy rainfall between Korea and the United States," *Weather and Climate Extremes*, vol. 37, p. 100490, Sep. 2022, doi: 10.1016/j.wace.2022.100490.
[16] Q. Dai, J. Zhu, S. Zhang, S. Zhu, D. Han, and G. Lv, "Estimation of rainfall erosivity based on WRF-derived raindrop size distributions," *Hydrology and Earth System Sciences*, vol. 24, no. 11, Art. no. 11, Nov. 2020, doi: 10.5194/hess-24-5407-2020.
[17] D. T. Meshesha, A. Tsunekawa, M. Tsubo, N. Haregeweyn, and F. Tegegne, "Evaluation of kinetic energy and erosivity potential of simulated rainfall using Laser Precipitation Monitor," *CATENA*, vol. 137, pp. 237–243, Feb. 2016, doi: 10.1016/j.catena.2015.09.017.
[18] K. G. Renard, *Predicting Soil Erosion by Water: A Guide to Conservation Planning with the Revised Universal Soil Loss Equation (RUSLE)*. U.S. Department of Agriculture, Agricultural Research Service, 1997.
[19] W. H. Wischmeier and D. D. Smith, *Predicting rainfall erosion losses:a guide to conservation planning*. United States: Department of Agriculture, Science and Education Administration, 1978. Accessed: Mar. 15, 2023. [Online]. Available: https://handle.nal.usda.gov/10113/CAT79706928
[20] H. Li, Y. Yin, Y. Shan, and Q. Jin, "Statistical Characteristics of Raindrop Size Distribution for Stratiform and Convective Precipitation at Different Altitudes in Mt. Huangshan," *Chinese Journal of Atmospheric Sciences*, vol. 42, no. 2, pp. 268–280, 2018, doi: 10.3878/j.issn.1006-9895.1705.16291.
[21] M. Löffler-Mang and J. Joss, "An Optical Disdrometer for Measuring Size and Velocity of Hydrometeors," *Journal of Atmospheric and Oceanic Technology*, vol. 17, no. 2, pp. 130–139, Feb. 2000, doi: 10.1175/1520-0426(2000)017<0130:AODFMS>2.0.CO;2.
[22] V. N. Bringi, C. R. Williams, M. Thurai, and P. T. May, "Using Dual-Polarized Radar and Dual-Frequency Profiler for DSD Characterization: A Case Study from Darwin, Australia," *Journal of Atmospheric and Oceanic Technology*, vol. 26, no. 10, Art. no. 10, Oct. 2009, doi: 10.1175/2009JTECHA1258.1.
[23] M. Le and V. Chandrasekar, "Raindrop size distribution retrieval from dual-frequency and dual-polarization radar," *IEEE Transactions on Geoscience and Remote Sensing*, vol. 50, no. 5, Art. no. 5, May 2012, doi: 10.1109/TGRS.2011.2167683.
[24] Q. Yang, Q. Dai, S. Zhang, K. Zhu, and L. Zhang, "Size distribution retrieval model for X-band dual-polarization radar in china incorporating various climatic and geographical elements," *IEEE Trans. Geosci. Remote Sensing*, vol. 60, pp. 1–17, 2022, doi: 10.1109/TGRS.2022.3168586.
[25] T. Iguchi *et al.*, "GPM/DPR Level-2 Algorithm Theoretical Basis Document V07A," 2021.
[26] W. A. Petersen, S. W. Nesbitt, R. J. Blakeslee, R. Cifelli, P. Hein, and S. A. Rutledge, "TRMM Observations of Intraseasonal Variability in Convective Regimes over the Amazon," *Journal of Climate*, vol. 15, no. 11, pp. 1278–1294, Jun. 2002, doi: 10.1175/1520-0442(2002)015<1278:TOOIVI>2.0.CO;2.
[27] Z. S. Haddad and K.-W. Park, "Vertical profiling of precipitation using passive microwave observations: The main impediment and a proposed solution," *Journal of Geophysical Research: Atmospheres*, vol. 114, no. D6, 2009, doi: 10.1029/2008JD010744.
[28] E. Gorgucci and L. Baldini, "Performance Evaluations of Rain Microphysical Retrieval Using Gpm Dual-Wavelength Radar by Way of Comparison With the Self-Consistent Numerical Method," *IEEE Transactions on Geoscience and Remote Sensing*, vol. 56, no. 10, pp. 5705–5716, Oct. 2018, doi: 10.1109/TGRS.2018.2824399.
[29] Y. Sun *et al.*, "Vertical Structures of Typical Meiyu Precipitation Events Retrieved From GPM-DPR," *Journal of Geophysical Research: Atmospheres*, vol. 125, no. 1, Art. no. 1, 2020, doi: 10.1029/2019JD031466.
[30] L. Wen, G. Chen, C. Yang, H. Zhang, and Z. Fu, "Seasonal variations in precipitation microphysics over East China based on GPM DPR observations," *Atmospheric Research*, vol. 293, p. 106933, Sep. 2023, doi: 10.1016/j.atmosres.2023.106933.

[31] M. Kendon *et al.*, "State of the UK Climate 2022," *International Journal of Climatology*, vol. 43, no. S1, pp. 1–83, 2023, doi: 10.1002/joc.8167.
[32] C. W. Ulbrich, "Natural variations in the analytical form of the raindrop size distribution," *Journal of Climate and Applied Meteorology*, vol. 22, no. 10, Art. no. 10, 1983.
[33] L. Ji *et al.*, "Raindrop Size Distributions and Rain Characteristics Observed by a PARSIVEL Disdrometer in Beijing, Northern China," *Remote Sensing*, vol. 11, no. 12, Art. no. 12, Jan. 2019, doi: 10.3390/rs11121479.
[34] J. Awaka, T. Iguchi, and K. Okamoto, "TRMM PR Standard Algorithm 2A23 and its Performance on Bright Band Detection," *Journal of the Meteorological Society of Japan*, vol. 87A, pp. 31–52, 2009, doi: 10.2151/jmsj.87A.31.
[35] M. Steiner, R. A. Houze, and S. E. Yuter, "Climatological Characterization of Three-Dimensional Storm Structure from Operational Radar and Rain Gauge Data," *Journal of Applied Meteorology and Climatology*, vol. 34, no. 9, pp. 1978–2007, Sep. 1995, doi: 10.1175/1520-0450(1995)034<1978:CCOTDS>2.0.CO;2.
[36] J. Zhu, S. Zhang, Q. Yang, Q. Shen, L. Zhuo, and Q. Dai, "Comparison of rainfall microphysics characteristics derived by numerical weather prediction modelling and dual-frequency precipitation radar," *Meteorological Applications*, vol. 28, no. 3, Art. no. 3, 2021, doi: 10.1002/met.2000.
[37] J. M. Valdivia, P. N. Gatlin, S. Kumar, D. Scipión, Y. Silva, and W. A. Petersen, "The GPM-DPR Blind Zone Effect on Satellite-Based Radar Estimation of Precipitation over the Andes from a Ground-Based Ka-band Profiler Perspective," *Journal of Applied Meteorology and Climatology*, vol. 61, no. 4, pp. 441–456, Apr. 2022, doi: 10.1175/JAMC-D-20-0211.1.
[38] K. Kanemaru, H. Hanado, and K. Nakagawa, "Improvement of the Clutter Removal Method for the Spaceborne Precipitation Radars," in *2021 IEEE International Geoscience and Remote Sensing Symposium IGARSS*, Jul. 2021, pp. 840–843. doi: 10.1109/IGARSS47720.2021.9554974.
[39] E. Peinó *et al.*, "Validation of GPM DPR Rainfall and Drop Size Distributions Using Disdrometer Observations in the Western Mediterranean," *Remote Sensing*, vol. 16, no. 14, Art. no. 14, Jan. 2024, doi: 10.3390/rs16142594.
[40] L. Liao, R. Meneghini, T. Iguchi, and A. Tokay, "Characteristics of DSD Bulk Parameters: Implication for Radar Rain Retrieval," *Atmosphere*, vol. 11, no. 6, Art. no. 6, Jun. 2020, doi: 10.3390/atmos11060670.
[41] L. Liao, R. Meneghini, and A. Tokay, "Uncertainties of GPM DPR Rain Estimates Caused by DSD Parameterizations," Nov. 2014, doi: 10.1175/JAMC-D-14-0003.1.

Jingxuan Zhu received the B.S. degree from Nanjing Normal University, Nanjing, China, in 2015, where she is currently pursuing the Ph.D. degree in cartography and geographical information system.
Her research interests include rainfall estimation and prediction based on radar remote sensing and rainfall kinetic energy and rainfall erosivity estimation on large scale.

Qiang Dai (Member, IEEE) received the Ph.D. degree in civil engineering from the University of Bristol, Bristol, U.K., in 2014.
He is a currently Professor with the School of Geography, Nanjing Normal University, Nanjing, China. His research interests are meteorology, hazards risk assessment, radar hydrology, and numerical weather prediction model. His key expertise within the center exists in meteorology, hazards, radar hydrology, and numerical weather prediction model.

Yuanyuan Xiao received the B.S. degree from Jiangxi Normal University, Nanchang, China, in 2022.
She is currently pursuing the Ph.D. degree in cartography and geographical information system from Nanjing Normal University, Nanjing, China. Her research interests include the relationship between rainfall and aerosols.

Jun Zhang received the Ph.D. degree in civil engineering from the University of Bristol, Bristol, U.K., in 2017.
She is currently an Associate Professor with the School of Geography, Nanjing Normal University, Nanjing, China. Her research interests are the simulation of water cycle in multiple scales and resolutions, groundwater simulations, urban flood.

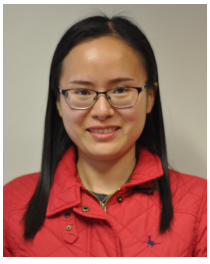

Lu Zhuo received the M.Eng. and Ph.D. degrees in civil engineering from the University of Bristol (UoB), Bristol, U.K., in 2011 and 2016, respectively.
She is currently working as a Lecturer with Cardiff University, Cardiff, UK. Her research interests include multiple natural hazards modelling and monitoring (e.g., floods, landslides, and earthquake), remote sensing of environment, and disaster risk management.

Dawei Han was born in Tianjin City, China, in 1961. He received the B.Eng. and M.Sc. degrees in water conservancy from the North China University of Water Conservancy and Electric Power, Zhengzhou, China, in 1982 and 1984, respectively, and the Ph.D. degree in radar hydrology from the University of Salford, Salford, U.K., in 1991.

He is currently a Professor of hydroinformatics with the Department of Civil Engineering, Uniersity of Bristol, Bristol, U.K. His research interests include hydroinformatics, real-time flood forecasting, flood risk management, remote sensing and geographic information system, natural hazards, and water resources management.